Structural basis for cargo binding and autoinhibition of Bicaudal-D1 by a parallel coiled-coil with homotypic registry

Shin-ichi Terawaki [a, d, *], Asuka Yoshikane [a, d], Yoshiki Higuchi [b, c, d], Kaori Wakamatsu [a, d]

[a] Graduate School of Science and Technology, Gunma University, 1-5-1 Tenjin-cho, Kiryu, Gunma 376-8515, Japan
[b] Department of Life Science, Graduate School of Life Science, University of Hyogo, 3-2-1 Koto, Kamigori-cho, Ako-gun, Hyogo 678-1297, Japan
[c] Department of Picobiology, Graduate School of Life Science, University of Hyogo, 3-2-1 Koto, Kamigori-cho, Ako-gun, Hyogo 678-1297, Japan
[d] SPring-8 Center, RIKEN, 1-1-1 Koto, Sayo-cho, Sayo-gun, Hyogo 679-5148, Japan

A B S T R A C T

Bicaudal-D1 (BICD1) is an α-helical coiled-coil protein mediating the attachment of specific cargo to cytoplasmic dynein. It plays an essential role in minus end-directed intracellular transport along microtubules. The third C-terminal coiled-coil region of BICD1 (BICD1 CC3) has an important role in cargo sorting, including intracellular vesicles associating with the small GTPase Rab6 and the nuclear pore complex Ran binding protein 2 (RanBP2), and inhibiting the association with cytoplasmic dynein by binding to the first N-terminal coiled-coil region (CC1). The crystal structure of BICD1 CC3 revealed a parallel homodimeric coiled-coil with asymmetry and complementary knobs-into-holes interactions, differing from Drosophila BicD CC3. Furthermore, our binding study indicated that BICD1 CC3 possesses a binding surface for two distinct cargos, Rab6 and RanBP2, and that the CC1-binding site overlaps with the Rab6-binding site. These findings suggest a molecular basis for cargo recognition and autoinhibition of BICD proteins during dynein-dependent intracellular retrograde transport.

© 2015 Elsevier Inc. All rights reserved.

1. Introduction

Cytoplasmic dynein plays an important role in sorting diverse cellular cargo during minus-end-directed intracellular transport along microtubules [1]. Recent studies revealed that five non-catalytic subunits link dynein to its cargo and to adaptor proteins that regulate dynein motor activity [2–6]. A structural analysis of the dynein motor domain revealed that its unique architecture generates force, allowing movement along microtubules [7–10]. However, the precise mechanism by which cytoplasmic dynein recognizes specific cargo remains unknown.

Bicaudal-D (BICD) proteins were first identified in Drosophila melanogaster as an adaptors for cytoplasmic dynein [11,12]. The Drosophila BicD protein and its mammalian homologues in cultured cells, BICD1 and BICD2, were predicted to be cytoplasmic α-helical coiled-coil (CC) proteins that primarily localized to the Golgi apparatus along with dynactin at microtubule plus ends [13]. BICD proteins possess three CC regions, a N-terminal CC1, a central CC2,

and a C-terminal CC3 region [14]. The N-terminal region of BICD, containing the CC1 and a portion of the CC2 regions, associates with cytoplasmic dynein [13]. Recent studies showed that upon inter-action with the N-terminal region of BICD, dynein was converted from a non-processive to a highly processive motor [15,16]. The C-terminal CC3 region of BICD directly interacts with cargo such as the small GTPase Rab6, which is involved in the regulation of membrane traffic from the Golgi apparatus to the endoplasmic reticulum (ER), and Ran-binding protein 2 (RanBP2), which is a component of the nuclear pore complex [17–19]. The cargo-binding function of the CC3 region promotes association with cytoplasmic dynein by disrupting its autoinhibitory interaction with the N-terminal CC1 region [13,20,21].

Mutations that perturb minus-end directed transport driven by cytoplasmic dynein have been identified in both cytoplasmic dynein and human adaptor proteins [22]. Various mutations in the human BICD2 gene have been found in patients with dominant congenital spinal muscular atrophy (DCSMA) and lower extremity predominance (LED) [23]. Two mutations, S107L and R501P, located within the N-terminal region of BICD2, increase binding affinity to cytoplasmic dynein [24]. The E774G mutation, located in the BICD CC3 region, results in defective Rab6 binding [25]. A recent study

* Corresponding author. Fax: +81 277 30 1439.
  E-mail address: terawaki@gunma-u.ac.jp (S. Terawaki).

using *Bicd2* knockout mice suggested that BICD2 plays a key role in cerebellar development and function by linking dynein-dependent cargo trafficking to granule neuron polarization and migration [26].

Here, we report on the crystal structure of mouse BICD1 CC3. Our structural analysis revealed that BICD1 CC3 forms a parallel homodimeric coiled-coil with leucine-zipper like heptad repeat sequences. A comparison with *Drosophila* BicD CC3 indicated that the parallel coiled-coil was a conserved structural feature that exhibited asymmetry [27]. However, the knobs-into-holes packing of BICD1 CC3 is adapted to the equivalent heptad position, which differs from *Drosophila* BicD CC3. Furthermore, *in vitro* binding studies revealed that BICD1 CC3 possesses distinct binding sites for two classes of cargo, Rab6 and RanBP2. Our structural and biochemical studies provide valuable clues to understanding the cargo sorting functions of cytoplasmic dynein through BICD proteins.

2. Materials and methods

2.1. Sample preparation

Mouse BICD1 CC3 (residues 711-808) and a constitutively active mutant of Rab6 (Rab6Q72L; residues 8-175) were expressed in *Escherichia coli* cells and purified as previously described [28]. The GST-fused BICD1 CC1 region (residues 1-300) and the MBP-fused RanBP2 BBR-RanBD3 (residues 2143-2450) were expressed using pET49b (Novagen) and pOPINM (Addgene) plasmids in *E. coli*, respectively. These recombinant proteins were purified using a glutathione sepharose 4B column (GE healthcare) or amylose resin column (New England Biolabs). Further purification was performed using a Hitrap Q sepharose high performance column (GE healthcare). The purified proteins were concentrated using a Vivaspin 20 (Vivascience).

2.2. Structural determination

Using X-ray diffraction data [28], the positions of 8 selenium sites were determined using SHELX-D [29]. The initial phase calculation and density modification were performed using SHARP and SOLOMON, respectively [30,31]. Model building was carried out from the calculated electron density map using the graphics program, COOT [32]. The structure was refined using the simulated annealing method and the TLS refinement method using the program PHENIX [33]. The structure contained additional N-terminal residues (3 and 1 residues for chain A and chain B, respectively). No model was built for the five C-terminal residues (residues 804-808) of chain B.

2.3. Pull-down assay of BICD1 CC3 with cargo factors and BICD1 CC1

To generate the MBP-fused BICD1 CC3 (MBP-BICD1 CC3) and Rab6Q72L complex, a solution containing 100 μM MBP-BICD1 CC3 and 100 μM Rab6Q72L was prepared and incubated at 277 K for 1 h in the pull-down buffer (10 mM Na-HEPES buffer pH 7.5, 150 mM NaCl, 1 mM DTT) containing 1 mM GTP and 5 mM MgCl$_2$. A complex solution containing 100 μM MBP-BICD1 CC3 and 100 μM of the RanBP2 BBR-RanBD3 fragment was prepared in the pull-down buffer. To reconstitute the autoinhibitory state of BICD1 CC3 bound to CC1, a solution containing 100 μM MBP- BICD1 CC3 and 200 μM CC1 was prepared in the pull-down buffer. These complexes were precipitated using amylose resin (New England Biolabs), which was equilibrated with the pull-down buffer. The resin-bound the complex was washed three times with 1 mL pull-down buffer and was eluted using 30 μl of the pull-down buffer containing 20 mM maltose. The amount of MBP-BICD1 CC3 and bound cargo, or BICD1 CC1, in each eluted solution was determined using SDS-PAGE.

3. Results

3.1. Structural determination and overall structure of BICD1 CC3

The BICD1 CC3 protein displayed high sequence homology to BICD2 and BicD (91% and 75% identity, respectively) and was predicted to contain 141 residues (residues 663-803) (Supplementary Fig. S1a). We prepared and crystallized the highly homologous CC3 region of mouse BICD1, which comprised 98 residues (residues 711-808). The structure of BICD1 CC3 was determined using the single-wavelength anomalous dispersion (SAD) method and was refined to 1.50 Å with an *R* value of 17.5% (a free *R* value of 20.6%). The asymmetric unit of the crystal contained a parallel coiled-coil dimer of BICD1 CC3 formed by two extended α-helices which are ~150 Å in length (Fig. 1A). Pairwise superposition of 93 Cα-carbon atoms (residues 711-803) between two helices displayed a large root-mean-square (r. m. s.) deviation of 2.9 Å. The structural difference between the two α-helices in the CC3 dimer is ascribed to the bending of the one helix (A chain), compared with a rather straight structure of the other helix (B chain) (Supplementary Fig. S1b). Thus, no structural symmetry of the α-helices of the CC3 dimer was maintained. The crystallographic statistics are summarized in Supplementary TableS1.

3.2. Parallel coiled-coil of BICD1 CC3

BICD1 CC3 was formed by a characteristic heptad repeat consisting of seven residues typically denoted as *abcdefg*, with *a* and *d* residues, such as leucine, showing hydrophobic properties required for knobs-into-holes packing (Fig. 1B and Supplementary Fig. S2) [34]. The heptad registers within the BICD1 CC3 dimer were determined using the SOCKET algorithm, which automatically recognizes knobs-into-holes interactions [35]. The coiled-coil packing of BICD1 CC3 was assigned to 78 residues (residues 720-797), which were completely contained in ten heptad repeats and two regions at the N- and C-terminal ends (residues 720-723 and 794-797), partially composed of four positions, *defg* and *abcd*, respectively. Although the N-terminal region (residues 711-719) was not assigned as the heptad repeat, this region created an extended α-helical region and contributed to the formation of the homodimeric coiled-coil through hydrophobic contact using the Tyr713 side chain. Additionally, the Tyr713 side chain creates the hydrogen bonds with Glu716 (Supplementary Fig. S3). The coiled-coil packing interface was formed between equivalent residues of the two chains (Fig. 1B and Supplementary Fig. S2). Interestingly, the heptad repeat arrangement in BICD1 CC3 was found to differ from the heterotypic knobs-into-holes packing interaction of BicD CC3 (Fig. 1C and Supplementary Fig. S2).

3.3. Comparison of homodimeric interactions in BICD1 CC3 and BicD CC3

To elucidate the differences in the heptad repeat arrangement of BICD1 CC3 compared to BicD CC3, we performed a superposition analysis. The superposition of BICD1 chain B (residues 734-780) with BicD chain A (residues 677-723) revealed that chain A of BICD1 shifted toward the N-terminus at an average of 3.8 Å, compared with the position of BicD CC3 chain D (Fig. 2A). The large displacement of BICD1 CC3 chain A was detected in four N-terminal heptad repeats (residues 724-752) and two, C-terminal heptad repeats (residues 787-794). The structural deviation between BICD1 CC3 and BicD CC3 may be caused by characteristic knobs-into-holes interactions of specific residues in BICD1.

The N-terminal region of BICD1 CC3 maintained a homodimeric interface by complementary packing interactions between
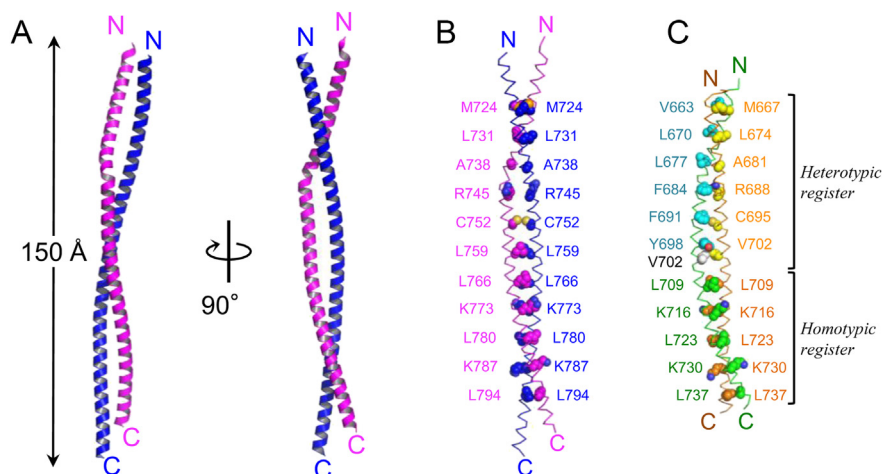
Fig. 1. Structure of BICD1 CC3 with homotypic registry. (A) The BICD1 CC3 homomeric dimer represented as a ribbon structure. Two polypeptide chains are colored in magenta and blue. (B) The homotypic knobs-into-holes interactions in BICD1 CC3. The residues forming *a* layers in the BICD1 CC3 structure are shown with wireframe representations of the main chains, and each chain is colored in magenta and blue. (C) Heterotypic BicD CC3 knobs-into-holes interactions. The N-terminal heterotypic register is offset by four amino acid sequence positions in each chain (colored in cyan and yellow). Val702, colored in black, is located in a noncomplementary position. Regions of the C-terminal homotypic register are colored in green and orange. (For interpretation of the references to colour in this figure legend, the reader is referred to the web version of this article.)

equivalent residues (Fig. 2B and D). Contact site I of BICD1 CC3 (residues 723-734) was created by knobs-into-holes interactions comprising *a* position residues, Met724 and Leu731, and *d* position residues, Leu727 and Leu734 (Fig. 2B). The *g* position residue, Glu730, contacting an *e* position residue, Lys735, formed salt

bridges. Similarly, contact site II was formed by homotypic knobs-into-holes interactions comprising the seven layers (Fig. 2D).

Three BicD CC3 aromatic residues, which are located at contact site II, were suggested to stabilize the asymmetric coiled-coil structure by inducing steric clash at the interhelical interface
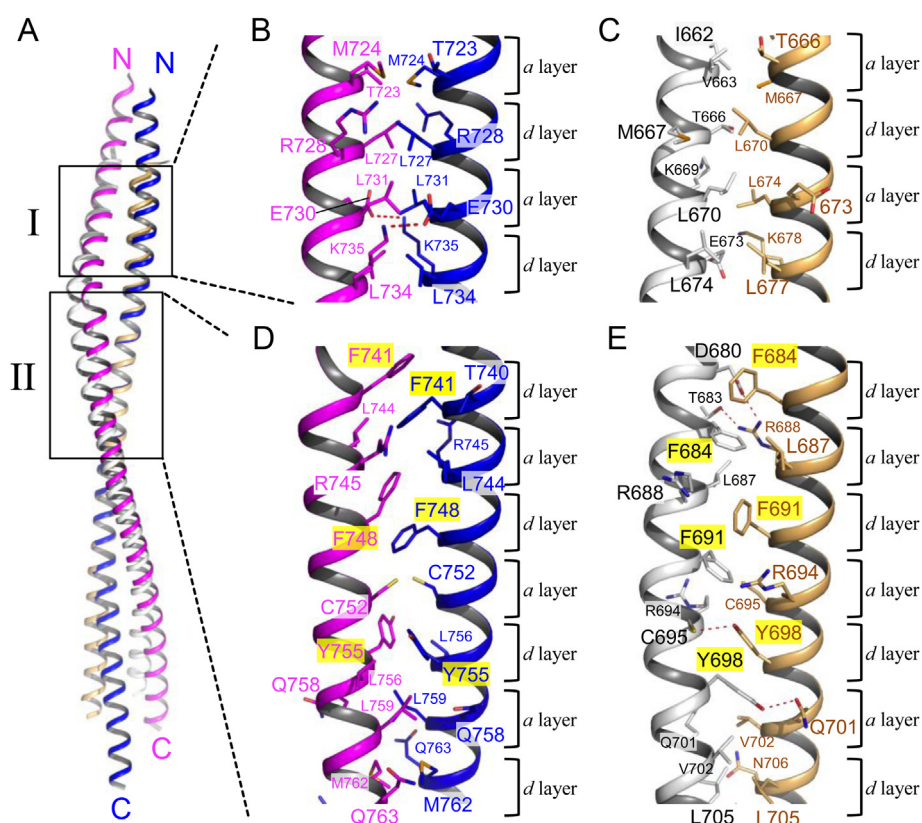
Fig. 2. Parallel coiled-coil packing of BICD1 CC3. (A) Comparison of BICD1 CC3 with BicD CC3 by pairwise superposition. The chain B of BICD1 CC3 (colored in blue) is superposed with chain A of BicD CC3 (colored in wheat). BICD1 chain A and BicD chain D are shown in magenta and white, respectively. Boxed regions indicated the heterotypic regions of BicD CC3. A close-up view of coiled-coil packing in BICD1 Box I (B), and BicD (C), with stick models of side chains. The brackets show the layers of the knobs-into-holes packing. Electrostatic bonds are shown as red dashed lines. Coiled-coil packing in BICD1 Box II (D) and BicD (E). (For interpretation of the references to colour in this figure legend, the reader is referred to the web version of this article.)

(Fig. 2E) [27]. Structural analysis of BICD1 CC3 also revealed that two residues, Phe741 and Phe748, forming the *d* layers, stack the aromatic rings face-to-face between the two helices (Fig. 2D). In addition, the aromatic side chain of Tyr755 creates a complementary pairwise, type4 knobs-into-holes interaction (Fig. 2D) [35]. In contrast, the aromatic residues Phe684 and Phe691 of BicD, which correspond to Phe741 and Phe748 of BICD1 CC3, form a face-to-edge contact with aromatic rings between these side chains in a distinct layer (Fig. 2E). The side chains of BicD Tyr698 also interact by stacking aromatic rings face-to-face on the same molecular side.

3.4. Molecular surface properties of BICD1 CC3

BICD1 CC3 displays a characteristic electrostatic surface potential with a highly polarized distribution generated by positively charged N-terminal and negatively charged C-terminal regions (Fig. 3A). The positively charged surface, basic1, of the N-terminal region (residues 726-751) contains six basic residues, Lys726, Arg728, Lys732, Lys735, Arg745, and Arg751 (Fig. 3B and Supplementary Fig. S1a). In contrast, the C-terminal region possesses two negatively charged surfaces, acidic1 and acidic2, and contains a positive charged region, basic2, located between the two negatively charged surfaces. Acidic1 is a highly conserved region consisting of 38 residues (residues 753-772) (Fig. 3C and Supplementary Fig. S1a). The acidic2 region is created by four conserved acidic residues, containing Glu795 and Glu798. The electrostatic surface properties of BICD1 CC3 are similar to the molecular surface properties of BicD CC3 (Fig. 3D).

3.5. Interaction of BICD1 CC3 with Rab6

We examined the interaction of the MBP-fused BICD1 CC3 (MBP-BICD1 CC3) fragment with a Rab6 constitutively active mutant, Rab6Q72L, by pull-down assay. Compared to wild type MBP-BICD1 CC3, truncation of the acidic2 region disrupted Rab6 binding (Fig. 4A). Furthermore, the three alanine-mutants (Glu772, Ile784, and Lys787) displayed a reduction in Rab6 binding affinity (Fig. 4B). In contrast, the Met782, Glu795, and Glu798 mutants did not show a detectable reduction. These results suggest that the

BICD1 C-terminal region (residues 753-800) plays an essential role in Rab6 binding, where the acidic1 and basic2 regions interact with Rab6 and the acidic residues in the acidic2 region are not required for the Rab6 binding.
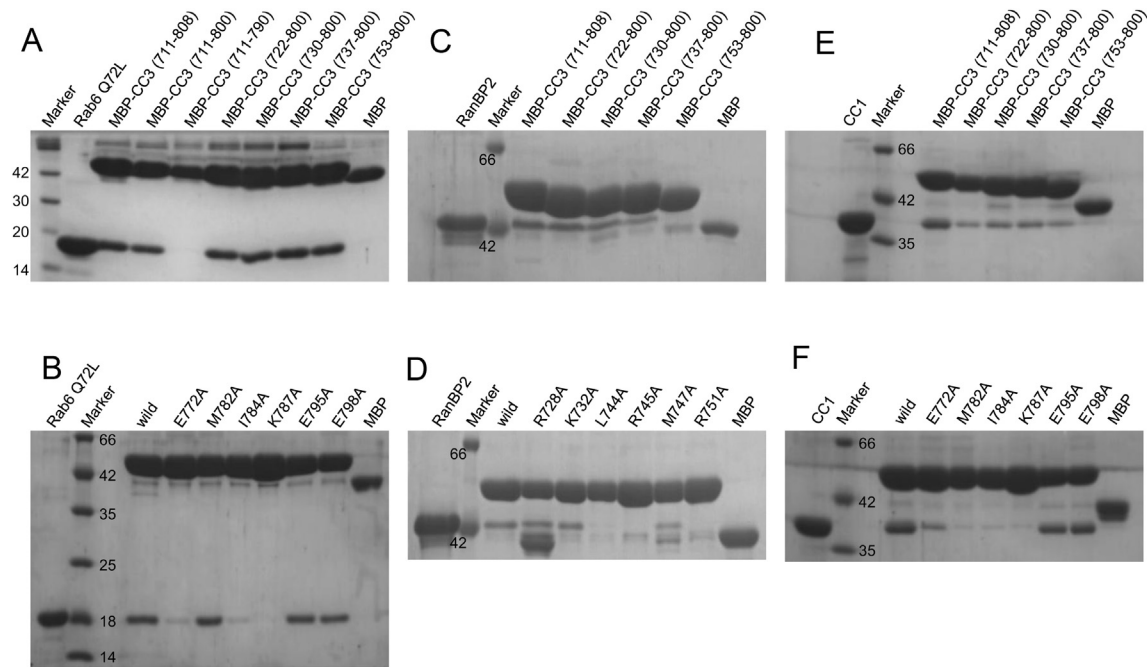
3.6. Interaction of BICD1 CC3 with RanBP2

RanBP2 is a giant protein comprised of 3224 residues. A recent study reported that the CC3 region of mouse BICD2 directly binds the linker region (residues 2143-2293) between two Ran-binding domains (RanBD2 and RanBD3), referred to as the BICD-binding region (BBR) [19]. To confirm whether BICD1 CC3 binds to the RanBP2 BBR, we performed a pull-down assay of MBP-BICD1 CC3 with purified BBR-RanBD3 (residues 2143-2450). We determined that RanBP2 BBR-RanBD3 bound to MBP-BICD1 CC3 (Fig. 4C); however, N-terminal truncation mutant (residues 753-800) showed a significant binding reduction. The three alanine-mutants (Leu744, Arg745, and Arg751) on the positively charged basic1 region displayed a reduction in RanBP2 binding affinity (Fig. 4D). These results strongly suggest that the N-terminal segment of BICD1 CC3 containing the positively charged basic1 region has a critical role in RanBP2 binding.

3.7. Intramolecular interaction of BICD1 CC3 with the N-terminal CC1 region

To determine the CC1 binding site, a pull-down assay using the MBP-BICD1 CC3 and the CC1 region was performed. The N-terminal truncation mutant (residues 753-800) exhibited a reduced CC1-binding affinity to 40%, but this was not a significant reduction (Fig. 4E). A pull-down assay using the four MBP-BICD1 CC3 point mutants, Glu772, Met782, Ile784, and Lys787 (that create the acidic1 and basic2 surfaces), showed a reduction in CC1 binding affinity; however the two residues of the acidic2 region, Glu795 and Glu798, showed no reduction in binding affinity (Fig. 4F). These results suggest that the C-terminal region, containing acidic1 and basic2 regions required for the Rab6-binding, may have an essential role in CC1 binding for the formation of an autoinhibitory state.
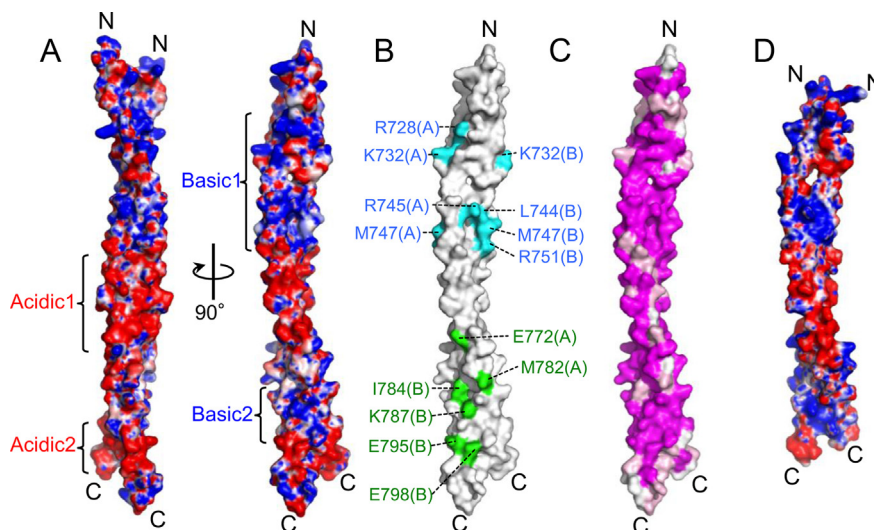
Fig. 3. Molecular surface properties of BICD1 CC3. (A) The surface electrostatic potential of the BICD1 CC3 dimer. Positive (blue: +10 kT/e) and negative (red: −10 kT/e) potentials are mapped on the molecular surface. (B) The position of mutated residues shown on the molecular surface are colored green for Rab6-binding and cyan for RanBP2-binding sites. (C) The conserved residues were mapped on the molecular surface. Conserved and semi-invariant conserved residues are colored in magenta and pink, respectively. (D) The surface electrostatic potential of BicD CC3. (For interpretation of the references to colour in this figure legend, the reader is referred to the web version of this article.)

Fig. 4. Interaction of BICD1 CC3 with cargo factors, Rab6 and RanBP2, and CC1. (A) Pull-down assay of MBP-BICD1 CC3 fragments with Rab6Q72L. The C-terminal truncation of 790-800 residues disrupted Rab6 binding. (B) Pull-down assay of MBP-BICD1 CC3 mutants with Rab6Q72L indicates a critical role of the acidic1 and basic2 regions in Rab6 binding. (C) Pull-down assay of MBP-BICD1 CC3 fragments with RanBP2 BBR-RanBD3. The deletion of the N-terminal basic1 region shows a significant binding reduction. (D) Pull-down assay of MBP-BICD1 CC3 mutants with RanBP2 BBR-RanBD3 suggests the essential role of the N-terminal basic1 region in RanBP2 binding. (E) Pull-down assay of MBP-BICD1 CC3 with CC1 suggests a key role of the CC3 C-terminal region in CC1 binding. (F) Pull-down assay of MBP-BICD1 CC3 mutants with CC1 indicates the overlap of the CC1-binding site with the Rab6-binding site.

4. Discussion

Our study showed that the BICD1 CC3 protein forms a parallel, homodimeric coiled-coil with axial asymmetry with complementary knobs-into-holes interactions between equivalent residues. The unique pairwise arrangement of three aromatic residues may play a key role in stabilizing this homotypic coiled-coil packing arrangement. The distinct conformation of the BICD1 Tyr755 side chain, compared to BicD Tyr698, results in a shorter inter-residue distance between its two α-helices (Supplementary Fig. S4). Although the heterotypic packing of BicD CC3 is stabilized by four electrostatic interactions at contact site II, the aliphatic residue in the next *a* layer might determine a preference for aromatic residue arrangement. The leucine residue is conserved in the *a* position following the *d* layer tyrosine in the mammalian BICD protein, whereas BicD has a valine residue at the same position (Supplementary Fig. S1a). This finding suggests the possibility that the presence of a bulky aliphatic side chain in the layer next to a tyrosine residue arranges aromatic residues in the homotypic registry by fixing the conformation of the tyrosine side chain.

Our binding experiments revealed that BICD1 CC3 has distinct binding sites for two classes of cargo, Rab6 and RanBP2. Although truncation of the acidic2 region disrupted Rab6 binding, mutating conserved acidic residues had no effect on Rab6 binding, suggesting that the acidic2 region contributes to the formation of the basic2 region by stabilizing coiled-coil packing, rather than providing a binding surface. In addition, the disruption of Rab6 binding *in vitro* caused by the Glu772 mutation located at the end of the acidic1 region, supported clinical research findings where the Glu774 mutation in human BICD2, corresponding to a mouse BICD1 Glu772 to glycine mutation, was observed in the genomes of patients suffering from DCSMA and LED and had an impairment in Rab6 binding [25]. Furthermore, we identified an N-terminal positive

region required for RanBP2 binding that was distinct from the C-terminal Rab6 binding site in BICD1 CC3. Our observation, indicating the existence of distinct sites for cargo-binding in a long coiled-coil structure, provides evidence that BICD proteins link many types of cargo to cytoplasmic dynein.

A previous report suggested the possibility that the CC1 release from the BicD CC3 region following cargo-binding is stimulated by a structural rearrangement of the knobs-into-holes core packing in a homodimeric coiled-coil [27]. A shift in the axial position of one helix in our BICD1 CC3 structure might show a transition between heterotypic and homotypic packing that involves autoinhibitory release. Furthermore, our binding study shows that three residues (Glu772, Ile784, and Lys787), required for Rab6 binding, play a critical role in the maintenance of the autoinhibitory state through direct interaction with the N-terminal CC1 region. The overlap of the Rab6-binding site with the CC1-binding site is assumed to simulate CC1 release from CC3 due to a competitive Rab6 binding effect and to stabilize the active state of BICD proteins by preventing CC1-binding.

Conflict of interest

None.

Acknowledgments

Appendix A. Supplementary data

Supplementary data related to this article can be found at http://dx.doi.org/10.1016/j.bbrc.2015.03.054.

Transparency document

Transparency document related to this article can be found online at http://dx.doi.org/10.1016/j.bbrc.2015.03.054.

References

[1] J.R. Kardon, R.D. Vale, Regulators of the cytoplasmic dynein motor, Nat. Rev. Mol. Cell Biol. 10 (2009) 854–865.

[2] K.T. Vaughan, R.B. Vallee, Cytoplasmic dynein binds dynactin through a direct interaction between the intermediate chains and p150Glued, J. Cell Biol. 131 (1995) 1507–1516.

[3] S. Karki, E.L. Holzbaur, Affinity chromatography demonstrates a direct binding between cytoplasmic dynein and the dynactin complex, J. Biol. Chem. 270 (1995) 28806–28811.

[4] A.W. Tai, J.Z. Chuang, C. Bode, U. Wolfrum, C.H. Sung, Rhodopsin's carboxy-terminal cytoplasmic tail acts as a membrane receptor for cytoplasmic dynein by binding to the dynein light chain Tctex-1, Cell 97 (1999) 877–887.

[5] A. Purohit, S.H. Tynan, R. Vallee, S.J. Doxsey, Direct interaction of pericentrin with cytoplasmic dynein light intermediate chain contributes to mitotic spindle organization, J. Cell Biol. 147 (1999) 481–492.

[6] M. Farkasovsky, H. Küntzel, Cortical Num1p interacts with the dynein intermediate chain Pac11p and cytoplasmic microtubules in budding yeast, J. Cell Biol. 152 (2001) 251–262.

[7] A.P. Carter, C. Cho, L. Jin, R.D. Vale, Crystal structure of the dynein motor domain, Science 331 (2011) 1159–1165.

[8] T. Kon, T. Oyama, R. Shimo-Kon, K. Imamula, T. Shima, K. Sutoh, et al., The 2.8 Å crystal structure of the dynein motor domain, Science 484 (2012) 345–350.

[9] H. Schmidt, E.S. Gleave, A.P. Carter, The 2.8 Å crystal structure of the dynein motor domain, Nat. Struct. Mol. Biol. 484 (2012) 345–350.

[10] H. Schmidt, R. Zalyte, L. Urnavicius, A.P. Carter, Structure of human cytoplasmic dynein-2 primed for its power stroke, Nature 518 (2014) 435–438.

[11] J. Mohler, E.F. Wieschaus, Dominant maternal-effect mutations of Drosophila melanogaster causing the production of double-abdomen embryos, Genetics 112 (1986) 803–822.

[12] R. Steward, C. Nüsslein-Volhard, The genetics of the dorsal-Bicaudal-D region of Drosophila melanogaster, Genetics 113 (1986) 665–678.

[13] C.C. Hoogenraad, A. Akhmanova, S.A. Howell, B.R. Dortland, C.I. de Zeeuw, R. Willemsen, et al., Mammalian Golgi-associated Bicaudal-D2 functions in the dynein-dynactin pathway by interacting with these complexes, EMBO J. 20 (2001) 4041–4054.

[14] M. Baens, P. Marynen, A human homologue (BICD1) of the Drosophila bicaudal-D gene, Genomics 45 (1997) 601–606.

[15] M.A. Schlager, H.T. Hoang, L. Urnavicius, S.L. Bullock, A.P. Carter, In vitro reconstitution of a highly processive recombinant human dynein complex, EMBO J. 33 (2014) 1855–1868.

[16] R.J. McKenney, W. Huynh, M.E. Tanenbaum, G. Bhabha, R.D. Vale, Activation of cytoplasmic dynein motility by dynactin-cargo adapter complexes, Science 345 (2014) 337–341.

[17] T. Matanis, A. Akhmanova, P. Wulf, E. Del Nery, T. Weide, T. Stepanova, et al., Bicaudal-D regulates COPI-independent Golgi-ER transport by recruiting the dynein-dynactin motor complex, Nat. Cell. Biol. 4 (2002) 986–992.

[18] B.F.J. Wanschers, R. van de Vorstenbosch, M.A. Schlager, D. Splinter, A. Akhmanova, C.C. Hoogenraad, et al., A role for the Rab6B Bicaudal-D1 interaction in retrograde transport in neuronal cells, Exp. Cell Res. 313 (2007) 3408–3420.

[19] D.L. Splinter, M.E. Tanenbaum, A. Lindqvist, D. Jaarsma, A. Flotho, K. Lou Yu, et al., Bicaudal D2, dynein, and Kinesin-1 associate with nuclear pore complexes and regulate centrosome and nuclear positioning during mitotic entry, Plos Biol. 313 (2007) 3408–3420.

[20] C.C. Hoogenraad, P. Wulf, N. Schiefermeier, T. Stepanova, N. Galjart, J.V. Small, et al., Bicaudal D induces selective dynein-mediated microtubule minus end-directed transport, EMBO J. 22 (2003) 6004–6015.

[21] D. Splinter, D.S. Razafsky, M.A. Schlager, A. Serra-Marques, I. Grigoriev, J. Demmers, et al., Mammalian Golgi-associated Bicaudal-D2 functions in the dynein-dynactin pathway by interacting with these complexes, Mol. Biol. Cell. 20 (2001) 4041–4054.

[22] J. Lipka, M. Kuijpers, J. Jaworski, C.C. Hoogenraad, Mutations in cytoplasmic dynein and its regulators cause malformations of cortical development and neurodegenerative diseases, Biochem. Soc. Trans. 41 (2013) 1605–1612.

[23] E.C. Oates, A.M. Rossor, M. Hafezparast, M. Gonzalez, F. Speziani, D.G. MacArthur, et al., Mutations in BICD2 cause dominant congenital spinal muscular atrophy and hereditary spastic paraplegia, Am. J. Hum. Genet. 92 (2013) 965–973.

[24] K. Neveling, L.A. Martinez-Carrera, I. Hölker, A. Heister, A. Verrips, S.M. Hosseini-Barkooie, et al., Mutations in BICD2, which encodes a golgin and important motor adaptor, cause congenital autosomal-dominant spinal muscular atrophy, Am. J. Hum. Genet. 92 (2013) 946–954.

[25] K. Peeters, I. Litvinenko, B. Asselbergh, L. Almeida-Souza, T. Chamova, T. Geuens, et al., Molecular defects in the motor adaptor BICD2 cause proximal spinal muscular atrophy with autosomal-dominant inheritance, Am. J. Hum. Genet. 92 (2013) 955–964.

[26] D. Jaarsma, R. van den Berg, P.S. Wulf, S. van Erp, N. Keijzer, M.A. Schlager, et al., A role for Bicaudal-D2 in radial cerebellar granule cell migration, Nat. Commun. 5 (2014) 3411.

[27] Y. Liu, H.K. Salter, A.N. Holding, C.M. Johnson, E. Stephens, P.J. Lukavsky, et al., Bicaudal-D uses a parallel, homodimeric coiled coil with heterotypic registry to coordinate recruitment of cargos to dynein, Genes. Dev. 27 (2013) 1233–1246.

[28] S. Terawaki, H. Ootsuka, Y. Higuchi, K. Wakamatsu, Crystallographic characterization of the C-terminal coiled-coil region of mouse Bicaudal-D1 (BICD1), Acta Crystallogr. F. Struct. Biol. Commun. 70 (2014) 1103–1106.

[29] T.R. Schneider, G.M. Sheldrick, Substructure solution with SHELXD, Acta Crystallogr. D. Biol. Crystallogr. 58 (2002) 1772–1779.

[30] G. Bricogne, C. Vonrhein, C. Flensburg, M. Schiltz, W. Paciorek, Generation, representation and flow of phase information in structure determination: recent developments in and around SHARP 2.0, Acta Crystallogr. D. Biol. Crystallogr. 59 (2003) 2023–2030.

[31] J.P. Abrahams, A.G.W. Leslie, Methods used in the structure determination of bovine mitochondrial F1 ATPase, Acta Crystallogr. D. Biol. Crystallogr. 52 (1996) 30–42.

[32] P. Emsley, K. Cowtan, Coot: model-building tools for molecular graphics, Acta Crystallogr. D. Biol. Crystallogr. 60 (2004) 2126–2132.

[33] P.H. Zwart, P.V. Afonine, R.W. Grosse-Kunstleve, L.-W. Hung, T.R. Ioerger, A.J. McCoy, et al., Automated structure solution with the PHENIX suite, Methods Mol. Biol. 426 (2008) 419–435.

[34] A.N. Lupas, M. Gruber, The structure of alpha-helical coiled coils, Adv. Protein Chem. 70 (2005) 37–78.

[35] J. Walshaw, D.N. Woolfson, Socket: a program for identifying and analysing coiled-coil motifs within protein structures, J. Mol. Biol. 307 (2001) 1427–1450.